Materials & Design 238 (2024) 112720

Contents lists available at ScienceDirect

Materials & Design

journal homepage: www.elsevier.com/locate/matdes

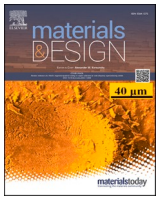

Laser powder bed fusion of $Fe_{60}(CoCrNiMn)_{40}$ medium-entropy alloy with excellent strength-ductility balance

Shengze Yang [a], Yang Liu [a,b,*], Hongyu Chen [a,b], Yonggang Wang [a,b], Konrad Kosiba [c]

[a] Faculty of Mechanical Engineering & Mechanics, Ningbo University, Ningbo 315211, China
[b] MOE Key Laboratory of Impact and Safety Engineering, Ningbo University, Ningbo 315211, China
[c] Leibniz Institute for Solid State and Materials Research Dresden, Institute for Complex Materials, Helmholtzstr. 20, 01069 Dresden, Germany

ARTICLE INFO

Keywords:
Laser powder bed fusion
High-entropy alloy
Heterostructure
Molecular dynamics
Synergistic strengthening and ductility

ABSTRACT

In this study, $Fe_{60}(CoCrNiMn)_{40}$ medium-entropy alloy (MEA) was fabricated by laser powder bed fusion (LPBF) via mixing of pure Fe and FeCoCrNiMn powders, the processability, microstructure and mechanical properties were systematically investigated, and the mechanism of strengthening and toughening were revealed through combination of experiments and molecular dynamics (MD) simulations. Results show that fraction of BCC phase decreased gradually with increasing volume energy density (VED), and thus heterostructue with varying FCC and BCC phases were produced through regulating the VED. The $Fe_{60}(CoCrNiMn)_{40}$ MEA (with scanning speeds of 700 and 800 mm/s) showed excellent strength-plasticity balance (e.g. 476 MPa, 612 MPa and 63 %) compared to the equiatomic FeCoCrNiMn HEA, which is ascribed to the synergistic strengthening and toughening effects involving the twinning induced plasticity (TWIP) and the reinforcement caused by the BCC phase (act as reinforced particle) embedded in the FCC matrix.

1. Introduction

Amongst metallic materials, medium/high-entropy alloys (M/HEAs) pose one new alloy concept which is in the focus of intense research efforts within recent years. The concept of M/HEA was first proposed by Ye et al. [1]. Subsequently, the FeCoCrNiMn HEA was firstly developed and studied by Cantor et al. [2]. The FeCoCrNiMn HEA shows attractive mechanical properties readily characterized by an excellent combination of strength and toughness [3], resistance to low temperature [4] and high strain hardening ability [5]. However, the widespread use of the FeCoCrNiMn HEA has been limited due to the following reasons: (1) The conventional fabrication methods of HEAs, for instance melt-casting and powder metallurgy, tend to result in the formation of Mn/Cr segregation compounds, which deteriorate the mechanical properties [6]. (2) Compared to commonly used metals like stainless steel, HEAs are composed of more costly elements [7].

For the past 20 years, the development of additive manufacturing (AM) technologies has made up for the vacancy of conventional fabricating methods to a large extent [8–10]. Laser powder bed fusion (LPBF) is considered to be among the most promising additive manufacturing processes for metal components. By stacking powder layer by layer and selectively melting spatially localized volumes of the powder layer via a laser beam with small spot size, parts with high dimensional accuracy and geometrical complexity can be produced [11]. Extremely high cooling rate is able to inhibit the formation of undesired segregation due to kinetic constraints affecting the phase formation. On the contrary, such high cooling rate allows for higher solubility of the solute in the solid solution when compared to traditional casting [12]. In addition, thermal stress forms due to the layer-by-layer manner, whereby the heat is extracted through the underlying material which then experience a subsequent heat-treatment. As a result, the microstructure of LPBF-fabricated HEAs is characterized by the formation of columnar grains and equiaxed sub-structures [13]. These sub-structures are actually dislocation walls, which significantly contribute to enhancing the strength of the material [14–17]. Numerous studies have been conducted, corroborating the superior mechanical characteristics of FeCoCrNiMn alloys fabricated through LPBF [18–22].

However, there is still room for improvement and the implementation of measures to enhance the performances of FeCoCrNiMn alloy. They can be divided into four categories: (a) addition of heterogeneous particles, (b) grain boundary engineering, (c) introduction of further phases and regulation of the phase content and (d) further adjustment of the HEA existing elements. The addition of high-melting particles such as TiC [23] and TiAl [24] can effectively improve the strength at the

* Corresponding author at: Faculty of Mechanical Engineering & Mechanics, Ningbo University, Ningbo 315211, China.
E-mail address: liuyang1@nbu.edu.cn (Y. Liu).

https://doi.org/10.1016/j.matdes.2024.112720
Received 6 June 2023; Received in revised form 28 January 2024; Accepted 29 January 2024
Available online 1 February 2024

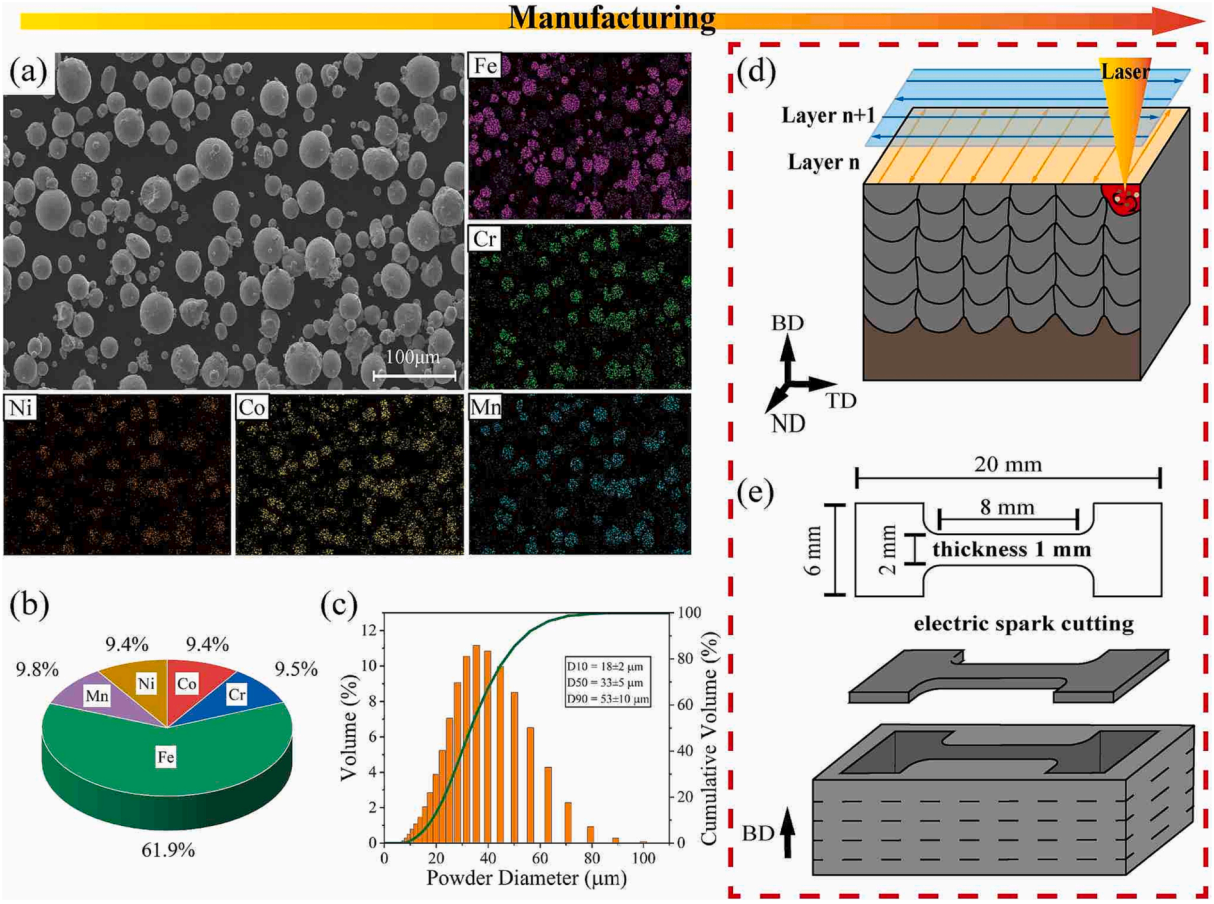

Fig. 1. (a) SEM and corresponding EDS elemental mapping of the powder mixture. (b) The proportion of elements in the mixed powder. (c) Particle size distribution of the powder after mixing. (d) LPBF laser scanning strategy and (e) geometry of the tensile sample.

expense of elongation. Given that FeCoCrNiMn primarily consists of a single face-centered cubic (FCC) phase [25], introducing Al is considered a feasible way to enhance its strength, because it is a body-centered cubic (BCC) phase stabilizer [26]. The BCC phase is typically harder than the FCC phase [27], the deformation incongruity between the both phases in the elastoplastic deformation can cause stress concentrations which in turn reduce the ductility of the material [28]. Moreover, the strength of the FeCoCrNiMn alloy composition has been effectively increased through modifications such as the addition of elements like Zr [29], removing Mn for more effective resistance against impact loads [30], or increasing the Fe content for enlarging the ductility [31]. These measures strengthened the FeCoCrNiMn HEA at the expense of other mechanical properties such as ductility. Therefore, strategies allowing for augmentation of one property of the FeCoCrNiMn HEA while not diminishing its other properties, are required and this is the motivation of the present work. Here, we altered the Fe content in FeCoCrNiMn and adopted LPBF to produce heterostructure. The processabilities under different energy inputs were studied, and the microstructure was characterized. In addition, the deformation and failure mechanisms are revealed by means of experimental characterization and molecular dynamic (MD) simulations.

2. Research details

2.1. Manufacturing process

Aerosolized pre-alloyed equiatomic FeCoCrNiMn and pure Fe powders (15–53 μm in diameter) were fabricated by Weilali New Material Technology Co., LTD. The two powders were mixed in 1:1 wt ratio using a planetary ball mill (NanDa Instrument QM-3SP4) at 200 rpm/min for 4 h. The micromorphology and plane distribution of the energy-dispersive X-ray spectroscopy (EDS) after mixing is depicted in Fig. 1a–c show the weight ratio of each element in the mixed powder and the particle size distribution of the powder, respectively. It is evident that the distribution of pure Fe and FeCoCrNiMn particles within the mixed powder is homogeneous. Additionally, the Fe element constitutes approximately 60 % of the overall composition. Moreover, the particle size distribution of the powder appears to be well-balanced and reasonable. This powder mixture was processed by LPBF with DiMetal-100H (Laser Additive Manufacturing GmbH, Guangzhou, China) and control power 200 W, layer thickness 30 μm and scanning spacing 70 μm unchanged, orthogonal scanning strategy was adopted to process the samples, as shown in Fig. 1d. The coordinate along the build direction (BD) and the other two directions are the normal direction (ND) and transverse direction (TD). The cuboid samples were processed into thin slices of dog bone-shaped tensile samples with a thickness of 1 mm by wire cutting (Fig. 1e). The length of the corresponding gauge section is 8 mm and the width is 2 mm.

2.2. Microstructure characterization

Samples were ground to mirror level prior to all testing. To test the relative density of the processed samples, measurements were performed in at least five replicates using the Archimedes drainage method. For phase identification, X-ray diffraction (XRD, STOE Stadi P, Cu Kα) was performed at 40 kV and 40 mA. The acquisition duration was set to 1°/min and the step size was 0.02°. A field emission scanning electron microscope (Gemini SEM 360, Zeiss Merlin) equipped with an electron

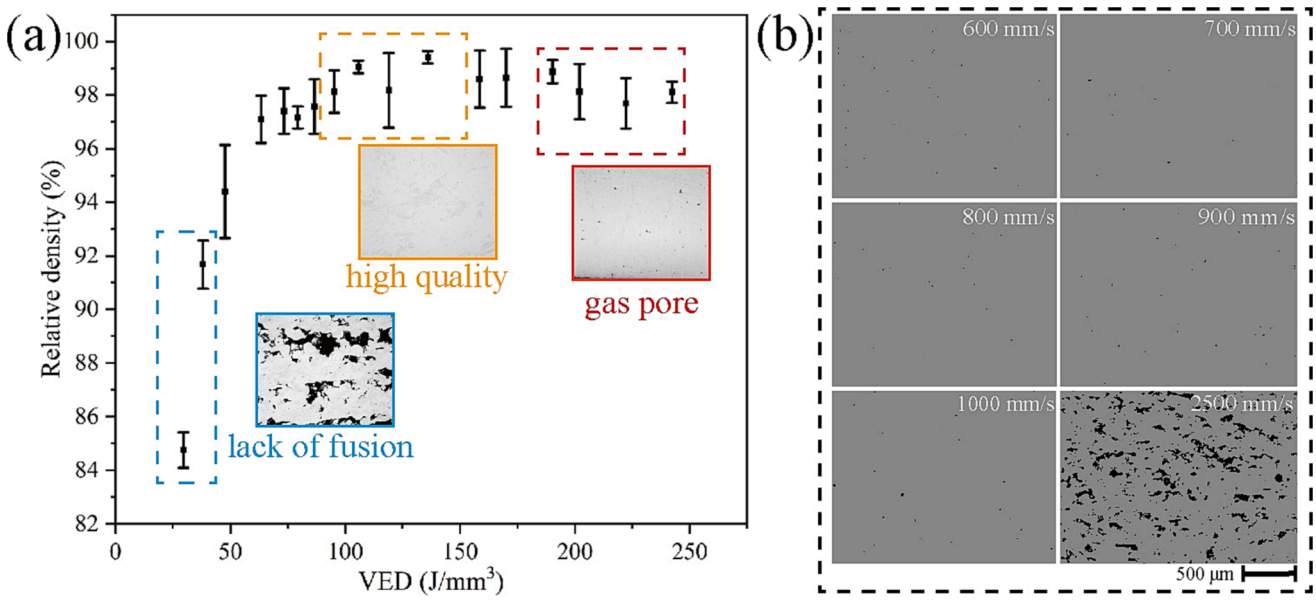

Fig. 2. Relative density (a) and porosity (b) at different scanning speeds.

backscatter diffraction (EBSD, Oxford Instruments) detector and energy dispersion spectrometer (EDS, Oxford Instruments) detector were endeavored to analyze the microstructure and determine the chemical composition. Prior to analysis by SEM, the samples were polished using diamond polishing fluid and afterwards corroded by etch solution (HCl: HNO_3: H_2O = 3:1:4) for 20–30 s. Optical microscopy (OM, Zeiss Merlin) was used to observe the surface quality and porosity of the polished etched materials. The sample surface for the EBSD investigation was prepared using an argon ion polisher to obtain a stress-free surface. For more detailed microstructure analysis, the samples were first prepared by argon ion thinning and then studied using a high-resolution transmission electron microscope (HR-TEM, FEI Tecnai G2 F20) at 200 kV and also selected area electron diffraction (SAED) patterns acquired.

2.3. Tensile testing

Samples were subjected to uniaxial tensile loading at strain rate of 10^{-3}/s using a small electronic tension test device (Autograph AGS-X Serious, SHIMADZU, Japan). At least five samples of the same state were tested to provide reproducible results. The yield strength (YS), ultimate tensile strength (UTS) and elongation were determined for all tested samples.

2.4. Molecular dynamic simulation

Large-scale atomic/molecular massively parallel simulator (LAMMPS) [32] was adopted to simulate the tensile loading of nanoscale polycrystalline materials for disclosing the underlying deformation mechanism. The random polycrystalline/ polyphase FeCoCrNiMn model at nanometer scale was established by using the Voronoi method [33] in the Atomsk software. In order to describe the interactions between different elemental atoms in this system, the second nearest-neighbor modified embedded-atom method (2NN MEAM) potential function developed by Choi et al. [34] was utilized. Data files generated by LAMMPS were observed through OVITO [35]. The adaptive common neighbor analysis (ACNA) [36] and dislocation extraction algorithm (DXA) [37] were adopted to distinguish between different crystalline structures and visualize defects such as stacking faults and dislocations. The modeling details can be found in the supplementary material.

3. Results

3.1. LPBF-fabrication of $Fe_{60}(CoCrNiMn)_{40}$ MEA

The samples were fabricated by LPBF at different volume energy density (VED) which is defined as follows:

$$VED = \frac{P}{vht} \tag{1}$$

where P is the laser power (W), v is the scanning velocity (mm/s), h is the hatch spacing (μm) and t is the thickness of the powder layer (μm). Fig. 2a displays the relative density of those samples. Samples produced at lower VED (30–50 J/mm^3) showed the lowest relative density. Higher VED values led to the preparation of denser samples until a density-plateau for the VED ranging between 100 J/mm^3 and 150 J/mm^3, which was hence a suitable processing window for the LPBF-fabrication of dense sample, and further increasing VED resulted in samples with lower relative density. The corresponding defect type is therefore termed lack of fusion and it occurred in the ‘1regime highlighted with the blue rectangle in Fig. 2a. Then high VED creates unstable vapor depression that ultimately result in numerous gas pores [38] (Fig. 2a: red rectangle and insert). Fig. 2b displays the OM images at varying scanning speed, the corresponding samples were label as V600, V700, … and V2500. The V2500 sample is characterized by a large number of large and irregular-shaped pores, while the V800 sample is mostly dense with only marginal porosity.

3.2. Micromorphology of the $Fe_{60}(CoCrNiMn)_{40}$ MEA

Orthogonal scanning line strategy was used during LPBF, the microstructure is characterized by checkerboard shape on the solidified top surface and by columnar shape along the building direction, as shown in Fig. 3a. Phase identification was conducted using XRD on the samples fabricated at different scanning speeds as shown in Fig. 3b. Interestingly, the XRD pattern of the V600 sample presents only reflections which can be allocated to a single FCC phase, while the BCC phase formed for the samples fabricated at 800 mm/s and faster as well as for the powder. The reflections corresponding to the BCC phase intensified for samples fabricated at increasing scanning speed and were most pronounced for the initial powder. Next to the phase formation, the increase in the scanning speed also affects the morphology of the

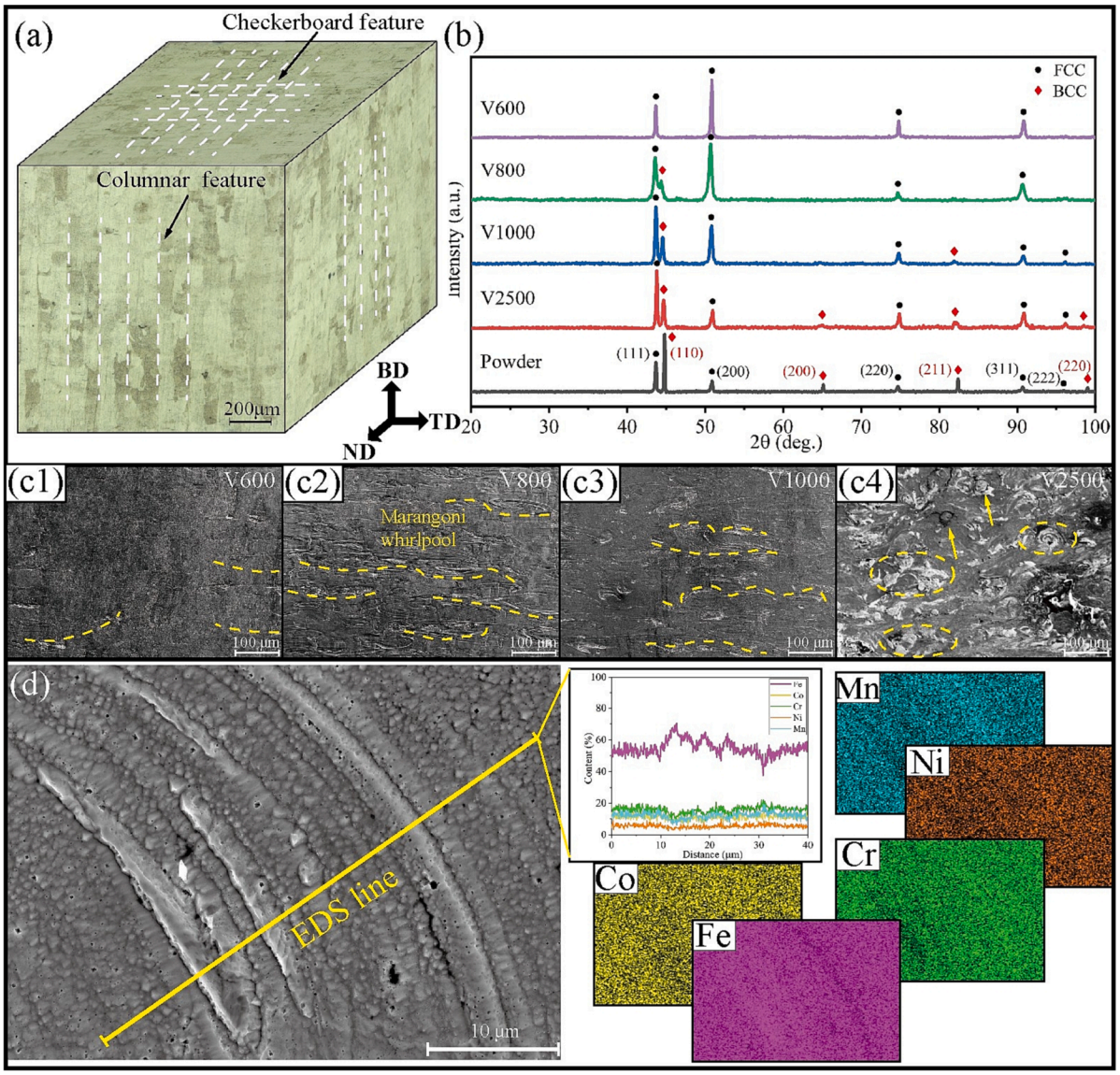

Fig. 3. (a) The 3D-OM image of V600 sample. (b) XRD patterns of samples with different scanning speeds. (c) SEM images of V600, V800, V1000 and V2500 samples on the plane perpendicular to BD. (d) SEM image, EDS line scanning maps of V800 sample.

microstructure, as the SEM images of the V600, V800, V1000 and V2500 samples along their building direction in (Fig. 3c1–4) disclose.

The extent of the solidified melt pools, which showed the "whirlpool"-like Marangoni pattern, as indicated by the yellow dotted lines in Fig. 3c1–4. With higher scanning speed, the extent of the Marangoni patterns decreased. These whirlpool-like patterns stem from the Marangoni effect [39] which lifts up the bottom of the melt pool volume, so that the surface-near melt is transferred downwards. The Marangoni flow facilitates the particles to fully melt by dragging them down into the melt pool [40], so that pure Fe and FeCoCrNiMn particles should diffuse and mix. This mixing should depend on the intensity and duration of the Marangoni flow is which is, however, determined by the processing parameters, since the flow is ultimately terminated when the melt pool has solidified. The Marangoni flow lasts then shorter when LPBF with processing parameters characterized by low VED values, e.g. fast scanning speeds is employed. Consequently, LPBF of the $Fe_{60}(CoCrNiMn)_{40}$ MEA powder mixture at the highest scanning speed of 2500 mm/s (he lowest VED), led in the present case to limited melting and hence limited diffusion of Fe particles within the CoCrNiMn melt (Fig. 3c4, yellow arrows).

Based on the above phenomenon, EDS line scanning was carried out in a close-up region in the solidified melt pool of the V800 sample. Fig. 3d displays the corresponding SEM image inclusive of EDS line scan, the corresponding elemental distribution and EDS maps. The SEM image shows brighter and darker, alternating regions which comprise a section of the Marangoni flow pattern. The apparent elemental distribution confirms this assumption. Brighter regions are enriched in Fe and depleted in the residual elements. In addition, widespread columnar/cellular substructures were observed in all samples, as shown in Fig. S1a. This is often seen in LPBF of FCC-metals and is actually composed of dislocation walls due to process residual stress [41], as demonstrated by TEM in Fig. S1b.

More detailed microstructure description involving texture and respective crystallographic texture of the samples are shown in Fig. 4. According to Fig. 4a1–e1, (001) crystal planes are widely present, which is due to the fact that the ⟨100⟩ directions of the face cubic center (FCC) structure grow more easily than the other directions during solidification [42]. By contrast, the grain growth of the V1000 sample is disturbed due to the excessive diffuse BCC phase. Moreover, The IPF figure and phase distribution of V2500 are shown in Fig. S2. The V2500 sample has numbers of lack-of-fusion holes, and the orientation is random. The phase distribution maps, presented in Fig. 4a2–b2, disclose

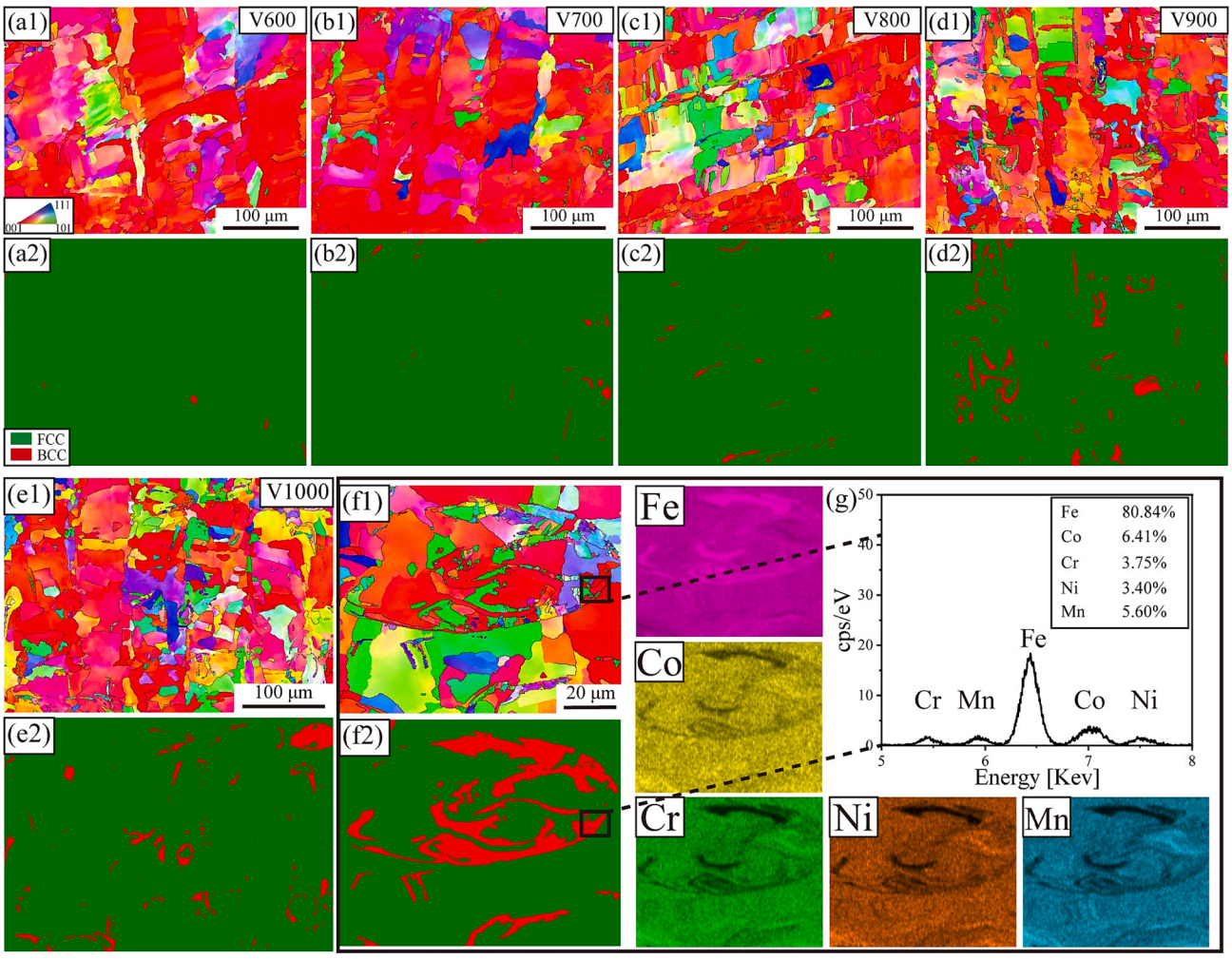

Fig. 4. IPF maps (a1–e1) and phase distribution (a2–e2) of the V600, V700, V800, V900 and V1000 samples. The f1, f2 and g illustrate the IPF map, phase distribution and TEM-EDS point scanning map of a close-up region in the V1000 sample.

the fraction of BCC phase content in the V600, V700, V800, V900, V1000 and V2500 (Fig. S2b) samples, which are 0.22 %, 0.76 %, 0.93 %, 4.2 %, 4.6 % and 22.5 %, respectively. Which indicated that as the VED decreases (scanning speed increases), the content of the BCC phase increases accordingly. Correspondingly, the grain size showed a decreasing trend. The averaged grain areas were 62.81, 48.94, 45.65, 42.53, 35.33 and 16.73 μm^2, respectively. Further, the locally magnified IPF map, phase distribution and EDS diagram of the BCC phase region of the V1000 sample are shown in Fig. 4f1, f2. The overall comparison shows that the grains in the BCC phase region are very fine (diameter 0.5 ~ 2 μm), with random orientation, and highly correlated with Fe content.

In addition, the BCC phase corresponds to Fe-riched area, the TEM-EDS point scanning map of the BCC region in V1000 shows that Fe content is about 80.84 %, while Co, Cr, Ni, Mn elements are 6.41 %, 3.75 %, 3.40 % and 5.60 %, respectively, as shown in Fig. 4g. In V2500 sample, there are regions with coarse grains fine grains in the BCC phase. The coarse-grained regions are spherical or blocky, while the fine-grained regions are Marangoni flow-like as shown in Figs. S2c, d. Lejček et al. [43] obtained randomly oriented single BCC with small average grain size (~5μm) in LPBF of pure Fe, which is very similar to our results. The grain refinement mechanism is thought to be the BCC-FCC-BCC transition during remelting, which occurs only at high Fe content. Hence, it can be concluded that these Marangoni flow-like fine-grained BCC phase is caused by the phase transition during the thermal cycle of LPBF. The increase of Fe reduces the stability of transition from FCC to BCC, especially when the content of Fe is higher than 60 %, the BCC phase is dominant [44]. Thus, higher VED (V600) promoted Fe diffusion, resulting in fewer BCC phase. In contrast, V1000 and V2500 samples contained more BCC phase. Polar figures (PF) of FCC and BCC phase for all samples (V600-V2500 for BCC phase) are shown in Figs. S3, S4, respectively. For the FCC phase, the (0 0 1) plane is the preferential orientation of all samples, but the texture intensity decreases with the increasing scanning speed, while the BCC phase is rather random.

3.3. Quasi-static tensile mechanical properties

Fig. 5a displays the quasi-static tensile engineering stress–strain properties of the $Fe_{60}(CoCrNiMn)_{40}$ MEA specimens fabricated at varying scanning speeds and additionally the FeCoCrNiMn HEA which serves as reference. The results generally demonstrate that the elongation of the $Fe_{60}(CoCrNiMn)_{40}$ MEA samples distinctly larger than of the equiatomic FeCoCrNiMn reference. By contrast, Fe addition to this equiatomic HEA results in decreasing YS but slightly increasing UTS. The exact LPBF-processing condition is decisive for the mechanical performance of the $Fe_{60}(CoCrNiMn)_{40}$ samples. Amongst them, the V600 sample exhibits the lowest YS and its mechanical behavior are a fitting example for the strength-ductility trade-off. In comparison to the FeCoCrNiMn reference, the V600 sample shows more than three times larger ductility at the expense of YS. V700 and V800 samples which surprisingly show simultaneous increase in strength and ductility when compared to the V600 sample. To be more precise, both samples show

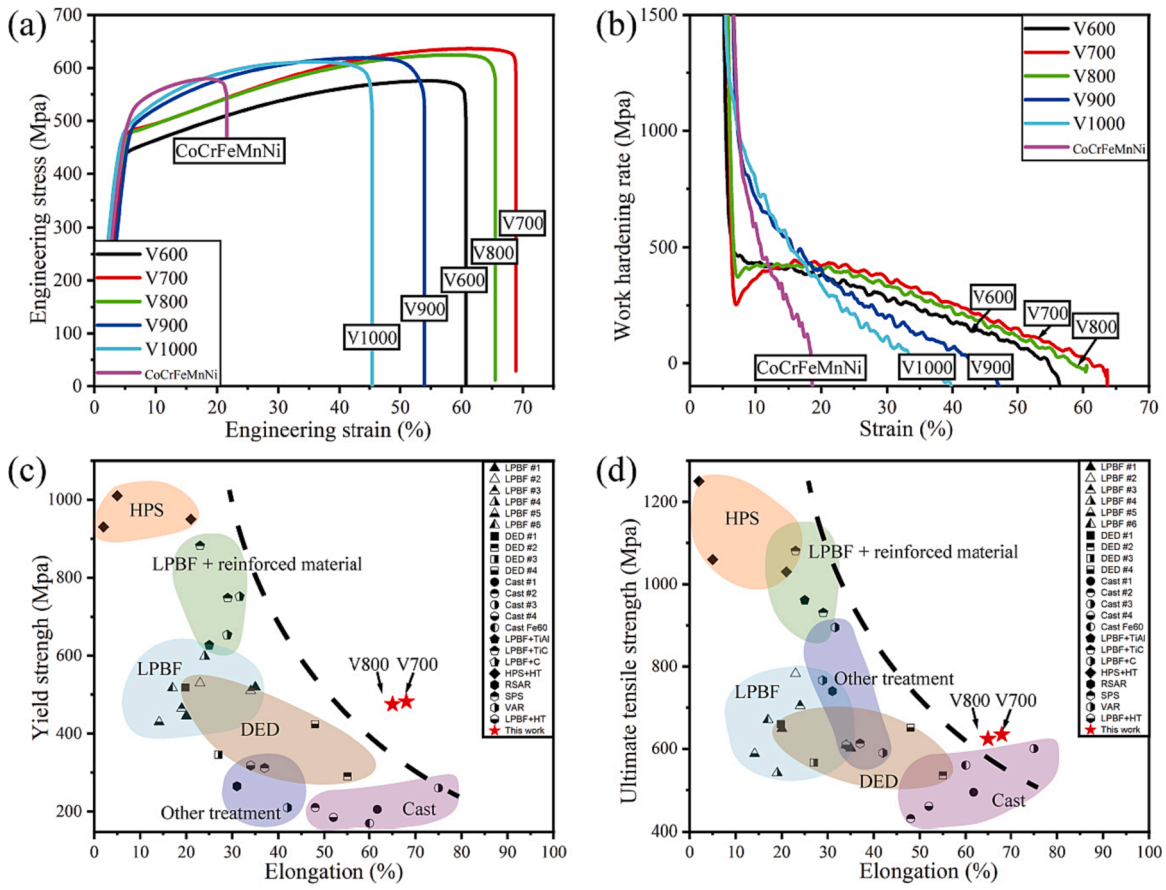

Fig. 5. Engineering stress–strain curves (a) and work hardening rate curves (b) of V600 to V1000 samples. A summary of yield strength-elongation (c) and ultimate tensile strength-elongation (d) in various FeCoCrNiMn-based alloys [19,23,24,4,44–60].

Table 1
Tensile mechanical properties of different samples.

Samples	YS (MPa)	UTS (MPa)	Elongation (%)
V600	417 ± 16	573 ± 36	58 ± 2
V700	472 ± 23	608 ± 30	68 ± 1
V800	476 ± 8	612 ± 18	63 ± 3
V900	482 ± 22	596 ± 37	49 ± 4
V1000	480 ± 11	612 ± 7	45 ± 2
FeCoCrNiMn	520 ± 21	584 ± 18	21 ± 3
LPBF-316L [61]	475	550	44 %
LPBF-316L [62]	510	630	42 %
LPBF-316L [63]	340	460	41 %

higher YS as well as UTS and an extended ductility. The application of even faster scanning speeds (V900 and V1000) in LPBF led to the synthesis of $Fe_{60}(CoCrNiMn)_{40}$ MEA samples with higher YS but lower ductility when compared to the V700 and V800 samples. Interestingly, Nokeun et al. [44] studied the performance of cast $Fe_{60}(CoCrNiMn)_{40}$, whose YS, UTS and elongation were about 170Mpa, 560Mpa and 60 %, respectively. The performance of the V700 and V800 samples was significantly higher than that of the cast counterparts, both in terms of strength and ductility. The reason will be discussed later. Moreover, in order to further quantify the mechanical responses, the work hardening rate (WHR) was calculated for each stress–strain curve, as shown in Fig. 5b. The WHR allowed to divide the deformation into three categories: The first is represented by the V600 sample, whereby the WHR firstly decreased in a steep manner followed by much less steep decrease at near-constant slope. The second is valid for the V700 and V800 samples. Thereby, the WHR rapidly decreased at first, then slightly increased ultimately followed by a decrease after crossing the local extremum WHR. The V900 and V1000 and equiatomic FeCoCrNiMn samples fell into the third category described by a gradually decreasing arc of the WHR. These deformation behaviors indicate three different microscopic deformation mechanisms under tensile loading and will be elaborated on later in the discussion section.

Table. 1 shows the mechanical properties of the samples prepared with different parameters and the comparison of 316L samples. It is worth mentioning that although the strength of V700 and V800 samples is slightly lower, the toughness is much higher than that of 316L, and the products of strength and elongation are 39.5 GPa% and 40.1 GPa%, respectively, which are significantly higher than 316L. Furthermore, the tensile properties of our LPBF-fabricated samples are compared to other FeCoCrNiMn-based HEAs prepared by various fabrication or post-treated methods including LPBF [19,23,45–48], direct energy deposition (DED) [49–52], cast [53–56], with addition of TiAl [24], TiC [23], C [57], high pressure torsion + heat treatment (HPS + HT) [58], rotary swaging and subsequent recrystallizaion (RSAR) [59], spark plasma sintering (SPS) [60], vacuum arc remelting (VAR) [4], LPBF + HT [46] and cast $Fe_{60}(CoCrNiMn)_{40}$ [44]. Fig. 5c, d illustrate the classification according to YS and elongation which highlights the superior strength-plasticity balance of the present $Fe_{60}(CoCrNiMn)_{40}$ MEA fabricated by LPBF.

3.4. Deformation-induced microstructural changes

Figs. 6a1-3, b1-3 and c1-3 display the BC, IPF and phase distribution maps of the V600, V800 and V1000 samples after loading, respectively. From the BC maps, one can observe that the V800 had the highest deformation twin (DT) density which may be expected, since this material provided the largest ductility. The IPF maps reveal that the

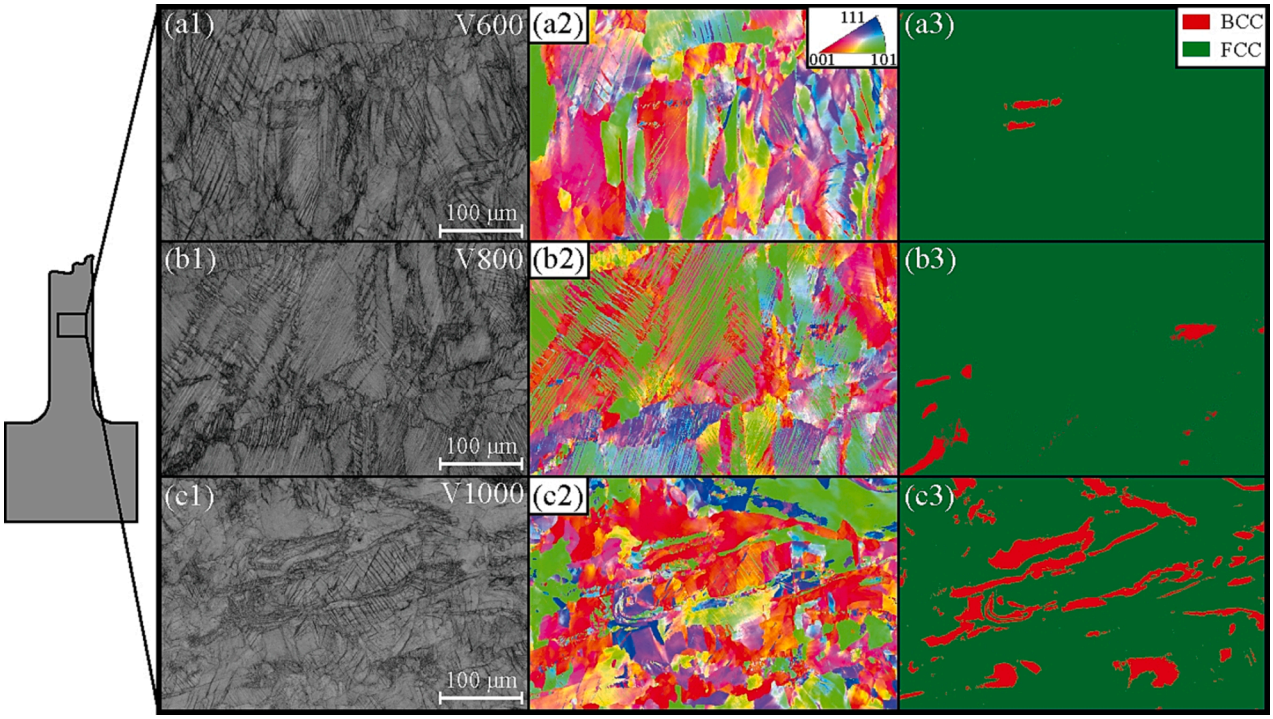

Fig. 6. Band contrast, IPF and phase distribution of the V600 (a1-3), V800 (b1-3) and V1000 (c1-3) samples in uniformly deformed regions.

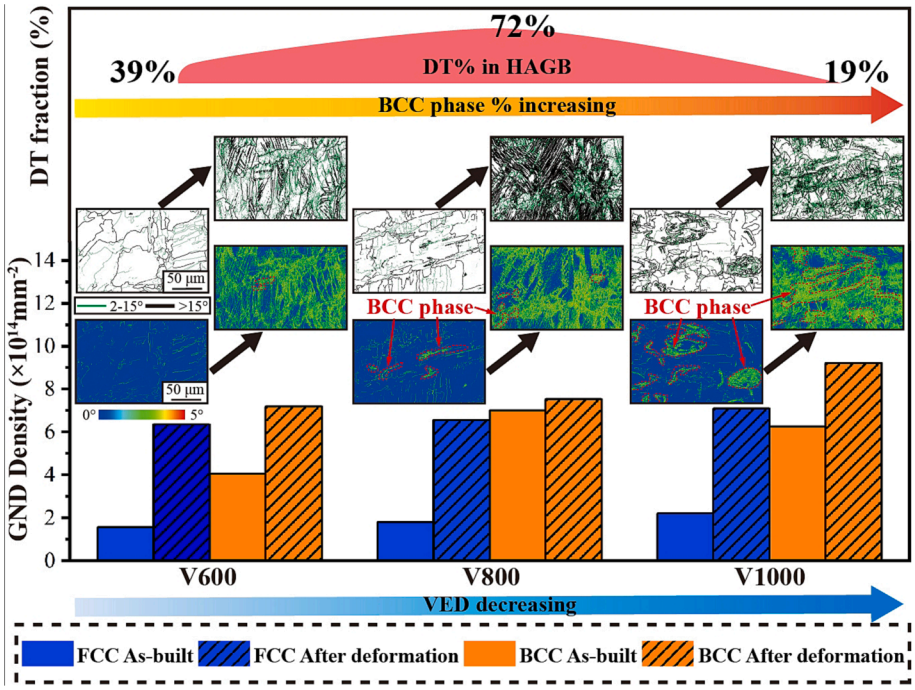

Fig. 7. The trend of the grain boundaries, KAM, DTs, and geometrically necessary dislocations (GNDs) within FCC and BCC phases before and after deformation.

number of the (0 0 1) plane of the deformed structure decreased after deformation when compared to the undeformed microstructure (Fig. 4a3, b3). This observation indicates the rotation of grains and the proliferation of twins during irreversible deformation. The combination of the phase and BC maps disclosed that DTs existed around the BCC phase in V800 and V1000 samples. However, it is not possible to determine whether these DTs initiate around the BCC phase or their growth stops when they encounter the BCC phase through these microscale observations after deformation. The responsible mechanism for their formation requires a further investigation.

4. Discussions

4.1. The role of DTs and BCC phase during deformation

Fig. 7 displays the trend of the grain boundaries, KAM, DT and geometrically necessary dislocations (GNDs) within FCC and BCC phases before and after deformation. According to the PFs of Figs. S3, S4, it can

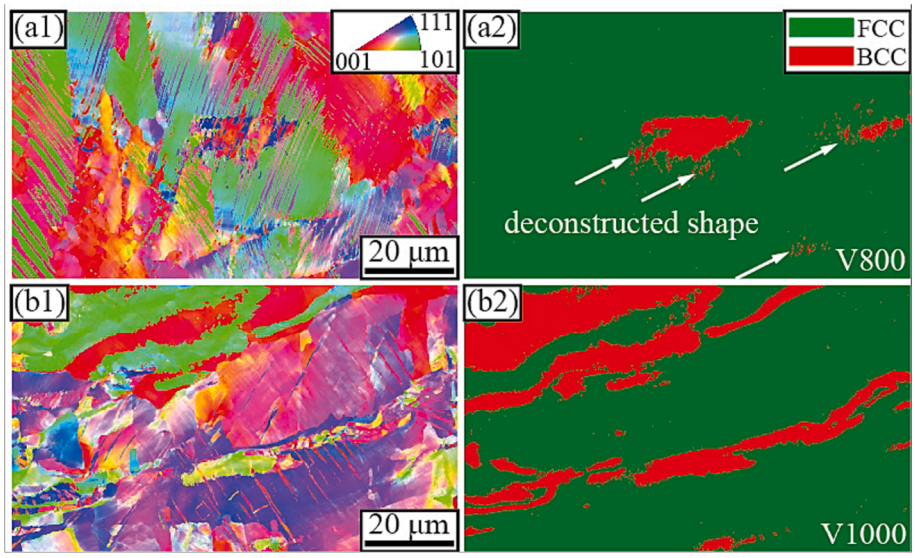

Fig. 8. Locally amplified IPF maps and phase distributions of the the V800 (a1-2) and V1000 (b1-2) samples after tensile deformation.

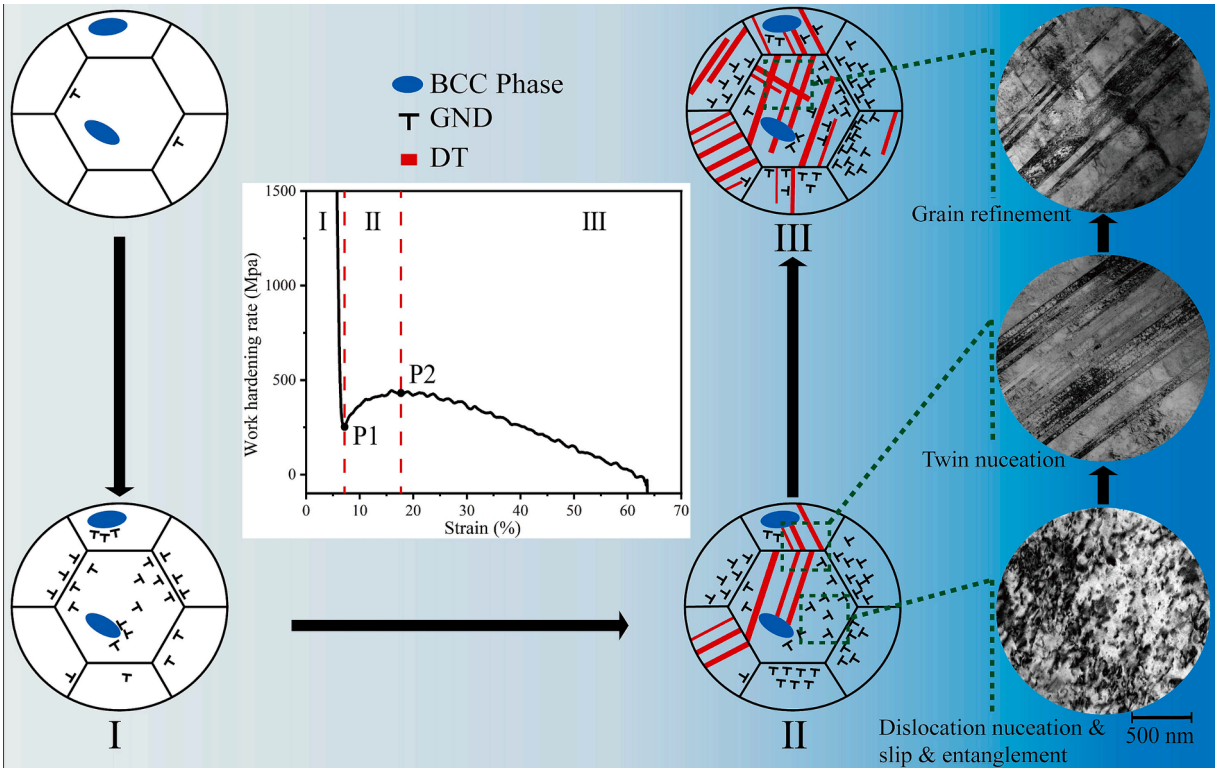

Fig. 9. Schematic diagram of the WHR evolution and its microscale mechanism effective in the LPBF-fabricated V700 and V800 samples.

be concluded that (0 0 1) is the preferential orientation and occupies a major proportion in the FCC phase of all samples. In addition, the orientation of the BCC phase is rather random and independent of the VED. Interestingly, the BCC phase of the all as-built samples showed denser grain boundaries associated with higher KAM value due to the BCC-FCC-BCC phase transition. It is well known that the phase transition of pure Fe can be achieved by local shuffling [64] or dislocation slip [43] during rapid heating or cooling, which is characterized by non-diffusion. Hence, a large number of slip-induced dislocations resulted in higher KAM value. The quantification GND density results showed that the dislocation density of the FCC phase varies greatly before and after deformation in all samples due to the severe deformation. In addition, the V800 sample contains up to 72 % DTs in HAGBs, while V600 and V1000 samples only contain 39 % and 19 % DTs, respectively. This indicates the possibility of TWIP effect in V800 sample.

The deformation behavior of the BCC phase, magnified sections of the IPF, phase distribution of the V800 and V1000 samples are displayed in Fig. 8a, b, respectively. It is worth noting that the BCC phase in the V800 sample shows a somehow “deconstructed” shape, as marked by the white arrow in Fig. 8a2. To be more precise, some fringed phase boundary decorated with isolated BCC phase regions inside the surrounding FCC grains is observed. In contrast, the BCC phase in the V1000 sample does not exhibit this shape (Fig. 8b2). This “deconstructed” shape of the BCC phase may be related to the severe plastic

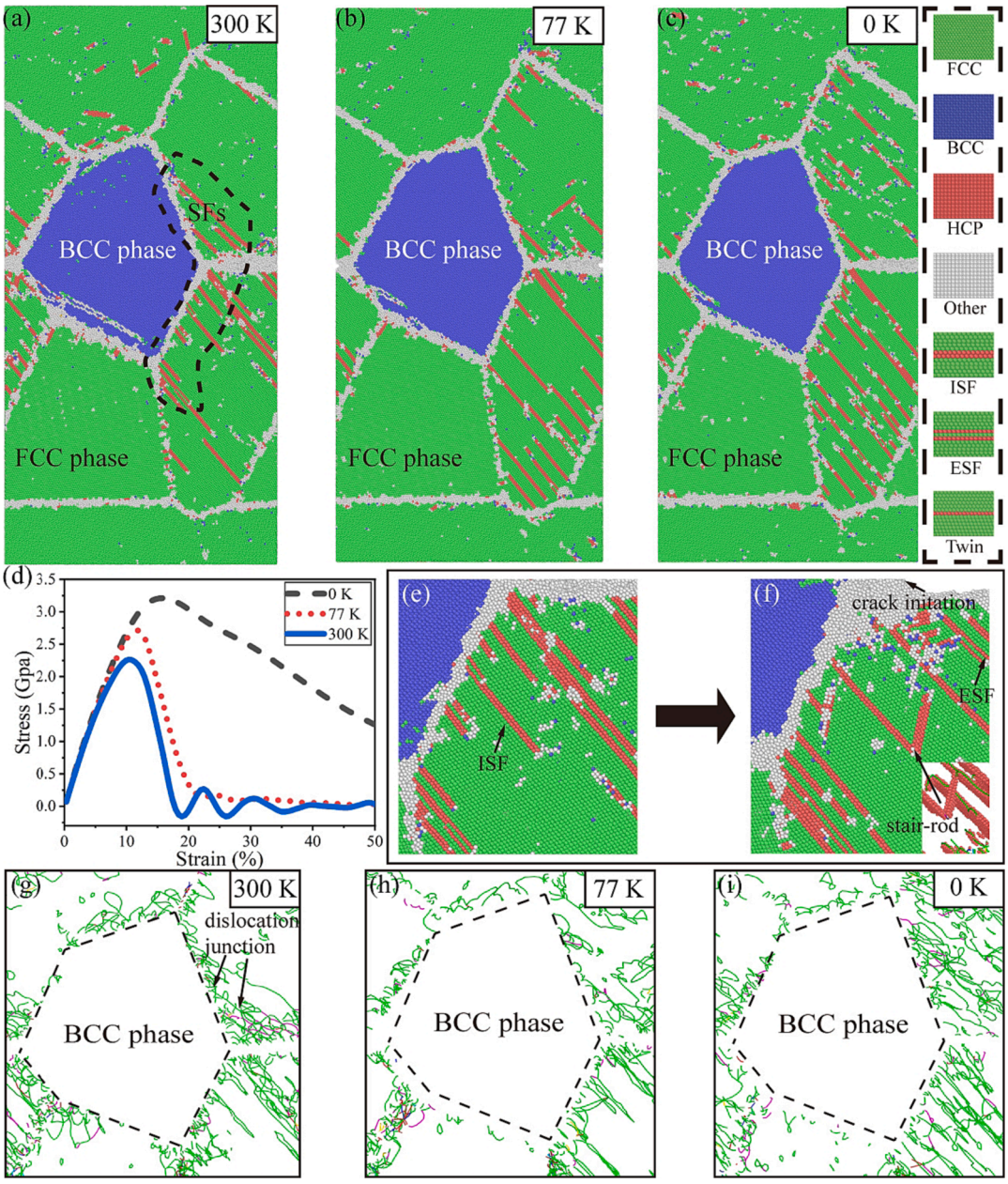

Fig. 10. MD simulation for tensile tests at temperatures of (a) 0 K, (b) 77 K and (c) 300 K, (d) Stress–strain curves of tensile simulations and (e-f) defect evolution near the BCC phase, (g-i) dislocation profiles in the interface area between the BCC and FCC phases at different temperatures.

deformation and evolution of stress concentration leading to the formation of DTs. It is well known that GNDs are blocked in BCC + FCC biphase alloys and hence accumulate at the phase interface during the elastoplastic deformation, thus back stress is generated in the FCC phase, while the BCC phase is subjected to forward stress [65]. In V1000 sample, higher proportion of the BCC phase bears more plastic deformation, thus, the TWIP effect induced by excessive stress concentration was avoided.

4.2. TWIP effect during plastic deformation

The V700 and V800 samples show peculiar WHR behavior (Fig. 5b) and in the following our aim is disclose the underlying deformation mechanism. The hardening stage of both samples can be divided into three stages (I, II and III), as is illustrated in Fig. 9. At first, the WHR monotonically dropped until at the minimum point P1 is reached which marks the end of stage I. Afterwards, the WHR increased until the maximum point P2 was reached (stage II) and subsequently gradually dropped again until fracture (III). Unlike other alloys which plastic deformation mechanism is dominated by dislocation and slip [66], the deformation mechanism of TWIP materials can be divided into several hardening stages: In the initial hardening stage (stage I), where DTs have not yet formed, the hardening is dominated by dislocation slip and entanglement. The storage rate of dislocations decreases as the microstructure is gradually saturated with dislocations. Meanwhile, dislocations began to be annihilated, eventually leading to decrease in the WHR. Due to the presence of smaller BCC phase content in the V700 and V800 samples, which forms a phase boundary with the FCC phase, dislocations will accumulate not only at grain boundaries but also near the BCC phase. Dislocation slip is often accompanied by the evolution of a large number of stacking faults. Indeed, the increase in the stacking fault density is believed to be conducive to the generation of DTs [67]. Therefore, in the later stage I, the formation of DTs set in and it caused the WHR to rise (stage II). Since plastic deformation is a continuous

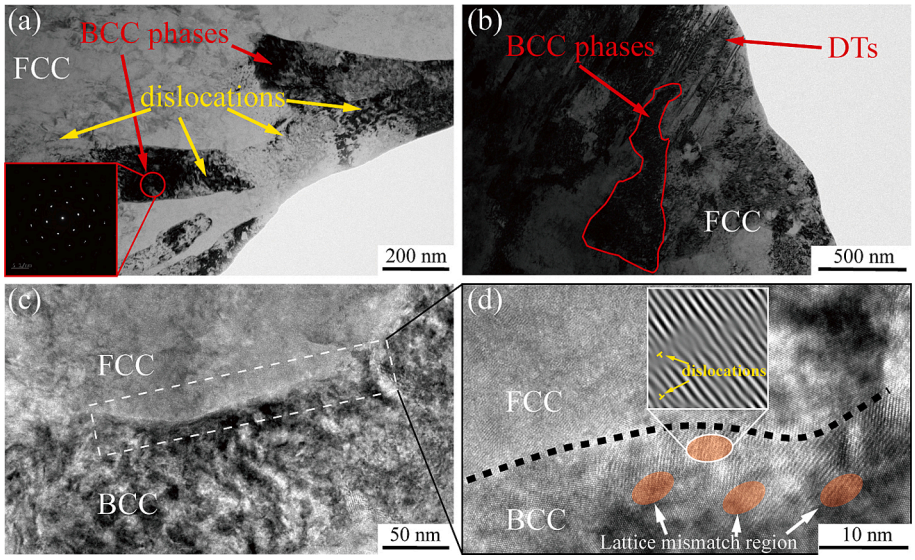

Fig. 11. TEM analysis of the deformed V800 sample. Dislocations (a), DTs (b) and HRTEM imaged (c, d) in the interface area between the BCC and FCC phases.

process, the nucleation and annihilation of dislocations occur simultaneously. Due to the very low nucleation rate of DTs, it will not be sufficient to cause an increase in the WHR, since the rate of dislocation annihilation may be greater than the generation of dislocations and DTs during work-hardening. Therefore, the rise of the WHR in stage II originates from a very high nucleation rate of DTs [68]. In general, in the present V700 and V800 samples, the interactions between dislocations, DTs and BCC phase regions mainly contribute to the enhancement of the WHR. With further increasing strain, a significant number of DTs and dislocation entanglements occur, resulting in grain refinement. This grain refinement, in turn, inhibits the generation of additional twins [69]. Finally, the WHR decreases then, since the rate of dislocation annihilation and detwinning is greater than the rate of twinning and dislocation nucleation (stage III) [70].

Therefore, two essential conditions must be met to obtain the WHR curve observed for the V700 and V800 samples (Fig. 9): (1) a sufficiently high twinning rate after dislocation slip and (2) a sufficiently high inter-defect interaction causing a high hardening rate. If only the first condition is met, the alloy will only elongate but no additional strengthening will occur. For example, in the cast $Fe_{60}(CoCrNiMn)_{40}$ with single FCC phase. the composition is homogeneous, a large number of DTs were induced during deformation, but they did not have effect on improving the strength [71], which is the same as V600 sample. In contrast, due to the little diffusion of Fe element, the V1000 sample contains a significant fraction of BCC phase, which prevents dislocation slips. However, the overall high SFE is not sufficient to produce DTs to lift plasticity. So, the present work demonstrates that appropriate process parameters allow to adjust the effective deformation mechanism by deliberate modulation of the fractions of the FCC and BCC phases, which is ultimately beneficial to the overall performance of the LPBF material.

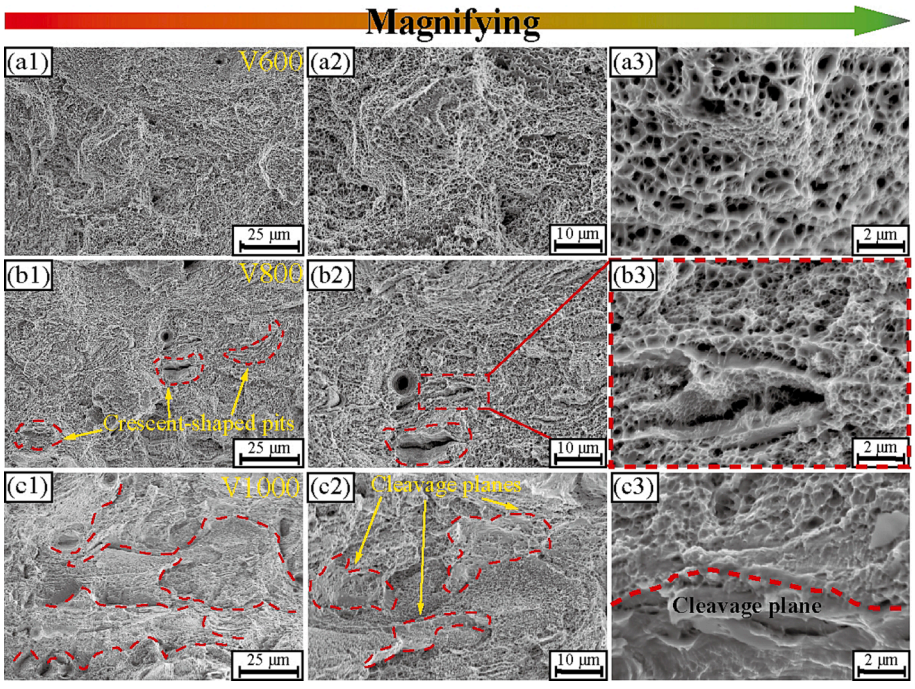

Fig. 12. Fracture surfaces of the V600 (a1-3), V800 (b1-3) and V1000 (c1-3) samples after tensile testing.

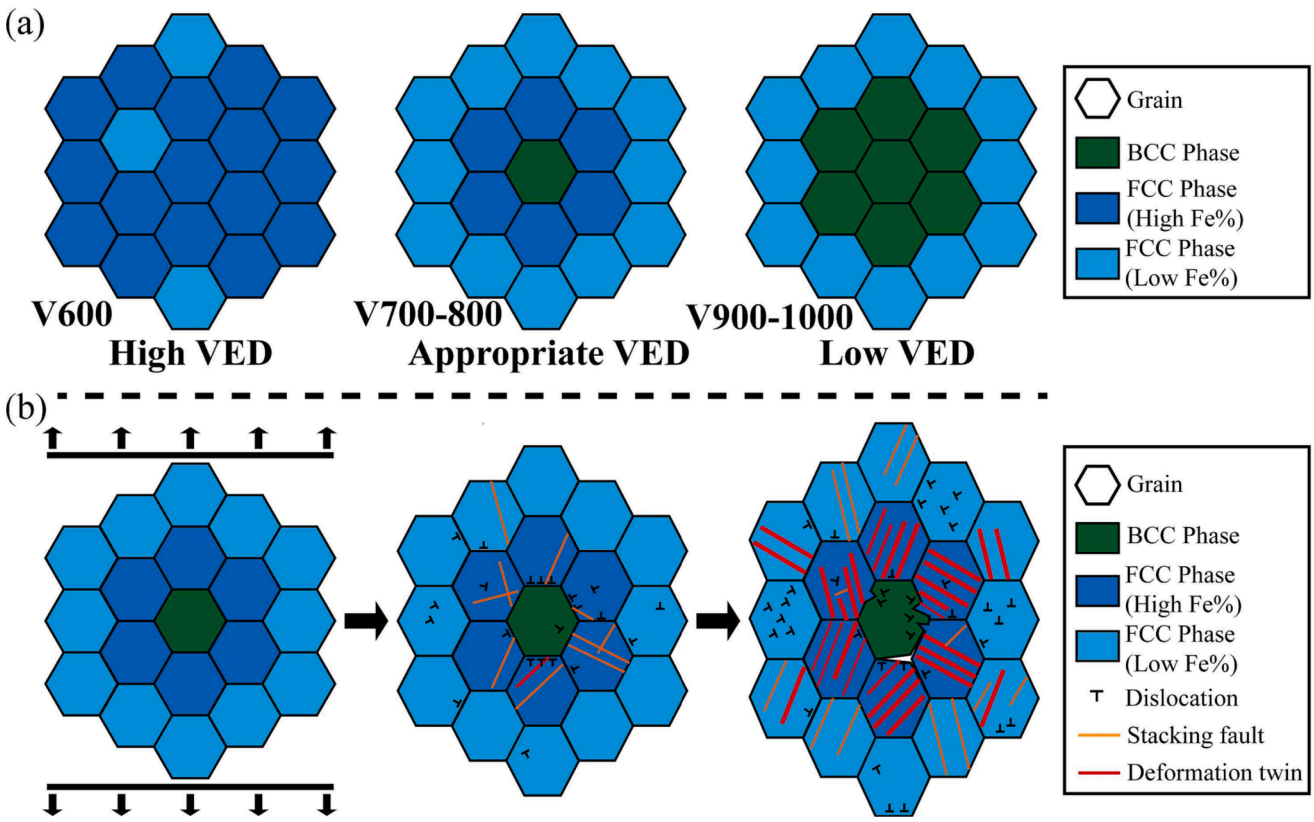

Fig. 13. (a) Effect of different VED on the microstructure of samples, (b) Schematic of the synergistic enhancement mechanism stemming from the TWIP effect and the heterogeneous structure in the V700 and V800 samples.

4.3. Strengthening mechanism due to the interaction of BCC and FCC phases

MD simulations were performed by using polycrystalline model containing FCC and BCC phases, and the results are shown in Fig. 10. When the strain was 12 %, the proportions of stacking faults (SFs) under 300 k, 77 k and 0 k were 2.5 %, 3.2 % and 3.8 %, respectively, as shown in Fig. 10a–c. At 300 K, SFs are mainly concentrated near the BCC phase due to the mismatch between the BCC and FCC phases with respect to the tensile deformation (Fig. 10a). However, this situation is improved at low temperature because the decrease of temperature reduces the SFE, thus leads to more SFs [72], the SFs are uniformly distributed in the grains, thus improving the overall strength of the sample (Fig. 10b, c). As shown in Fig. 10d, the lower the temperature, the higher the strength, which is related to the delayed failure caused by the uniform distribution of dislocations and SFs. When strain increased to 15 %, intrinsic stacking faults (ISFs) began to proliferate, some of which evolved into extrinsic stacking fault (ESFs), which are the primary form of DTs [73], as shown in Fig. 10e, f. Due to the mismatch of deformation, SFs interact with each other and form stair-rod dislocations, which play a strengthening role, as shown in Fig. 10f. Because the BCC phase is harder than the FCC phase, the BCC phase is always deformed slightly regardless of the temperature during the loading process, thus a large number of dislocations are generated around the BCC phase, as shown in Fig. 10g–i. Therefore, it can be concluded from the MD simulations that regardless of the temperature, the BCC phase can always exert strengthening effect by aggregating dislocations, which becomes stronger as the temperature decreases.

The deformed V800 sample was characterized by TEM, as shown in Fig. 11. Both dislocations and DTs were found at the phase boundaries, as shown in Fig. 11a, b, which is consist with EBSD results. According to the dislocation pinning theory, when dislocations are hindered by strengthening phase under deformation, the strengthening phase can pin the dislocations and prevent them from slipping further, leading to accumulation of dislocations [74]. Moreover, a large number of dislocations are also observed within the BCC phase, as shown in Fig. 11c, d, which indicates that stress was concentrated in BCC phase during deformation, leading to coordinating deformation of the BCC phase, which corresponds to the “deconstructed” shape of Fig. 8a.

The fracture surfaces of the V600 (a1-3), V800 (b1-3) and V1000 (c1-3) samples were analyzed via SEM (Fig. 12). All samples showed a ductile fracture pattern. Amongst them, the fracture surface of the V800 and V1000 samples showed crescent-shaped pits and cleavage planes (Fig. 12, red dash) in addition to a plethora of dimples. By considering the previous EBSD analysis and MD simulations, it can be concluded that these crescent-shaped pits are caused by the presence of the BCC phase. When the volume of the BCC phase is small (as in the V800 sample), the stress is more likely to concentrate near the BCC phase yielding a crescent-shaped crater after fracture (Fig. 12b2-3). Conversely, when the volume of the BCC phase is large (as in the V1000 sample), a fracture surface with characteristic cleavage pattern followed (Fig. 12c2). This observation is consistent with the tensile curves and prefer analysis.

4.4. Synergistic enhancement mechanism

Using VED allows for control over the degree of diffusion of pure Fe, thereby enabling regulation of the BCC phase in the $Fe_{60}(CoCrNiMn)_{40}$, among them, V700 and V800 samples showed excellent strength-ductility balance. We combine all previous analyses to give a schematic diagram shown in Fig. 13. During deformation, the grains in the Fe-riched regions begin to deform at first due to the lower SFE. Thereby, a large number of dislocations formed, stacking faults begin to slip and dislocation advance until the encounter dislocation walls, grain boundaries or the FCC/BCC phase boundaries (Fig. 13b). Owing to this obstruction, stress concentration is evolving which are subsequently alleviated by significant nucleation of DTs being tantamount to

deformation according to the TWIP mechanism. Further deformation leads to the formation of more dislocations, stacking faults, DTs and stress concentration. DTs are also induced within Fe-deficient regions (Fig. 13b, bright blue). Further deformation will lead to the initiation of cracks preferentially near the BCC phase, eventually leading to failure.

5. Conclusions

In this study, $Fe_{60}(CoCrNiMn)_{40}$ MEA was fabricated by LPBF via mixing of pure Fe and equiatomic FeCoCrNiMn powders, and the processability, microstructure, mechanical properties and deformation/failure mechanisms were discussed. The following conclusions can be obtained.

1) The pure Fe and FeCoCrNiMn powders were fused well by LPBF, the fraction of BCC phase decreased gradually with increasing VED, and thus produces heterostructure with varying FCC and BCC phases through regulating the VED.
2) The V700 and V800 samples showed excellent strength-plasticity balance compared to the equiatomic FeCoCrNiMn MEA.
3) The TWIP effect in combination with the presence of BCC phase embedded in the FCC matrix are responsible for the excellent strength-plasticity balance. Among them, the BCC phase provides the strengthening effect and the Fe-riched region provides TWIP effect.
4) MD results show that the uncoordinated deformation of BCC phase and FCC phase will lead to the mispacking of the SFs of FCC phase, which leads to the dislocation entanglement and finally the strengthening effect, which can be enhanced with the decrease of temperature.

CRediT authorship contribution statement

Shengze Yang: Writing – original draft, Investigation, Formal analysis, Data curation. **Yang Liu:** Writing – review & editing, Supervision, Funding acquisition, Conceptualization. **Hongyu Chen:** Methodology, Investigation, Funding acquisition, Formal analysis. **Yonggang Wang:** Writing – review & editing, Project administration, Funding acquisition. **Konrad Kosiba:** Writing – review & editing, Visualization, Validation, Investigation.

Declaration of competing interest

The authors declare that they have no known competing financial interests or personal relationships that could have appeared to influence the work reported in this paper.

Data availability

The authors do not have permission to share data.

Acknowledgments

This work was supported by the Natural Science Foundation of China (Grant No. 52375347), Natural Science Foundation of Ningbo (Grant No. 2023J008), Natural Science Foundation of Zhejiang (Grant No. LQ23E050010) and Postgraduate Research Innovation Fund of Ningbo University (Grant No. IF2023025).

Appendix A. Supplementary data

Supplementary data to this article can be found online at https://doi.org/10.1016/j.matdes.2024.112720.

References

[1] J.W. Yeh, S.K. Chen, S.J. Lin, J.Y. Gan, T.S. Chin, T.T. Shun, C.H. Tsau, S.Y. Chang, Nanostructured high-entropy alloys with multiple principal elements: novel alloy design concepts and outcomes, Adv. Eng. Mater. 6 (5) (2004) 299–303.
[2] B. Cantor, I.T.H. Chang, P. Knight, A.J.B. Vincent, Microstructural development in equiatomic multicomponent alloys, Mater. Sci. Eng. A 375–377 (2004) 213–218.
[3] G. Laplanche, O. Horst, F. Otto, G. Eggeler, E.P. George, Microstructural evolution of a CoCrFeMnNi high-entropy alloy after swaging and annealing, J. Alloy. Compd. 647 (2015) 548–557.
[4] A. Gali, E.P. George, Tensile properties of high- and medium-entropy alloys, Intermetallics 39 (2013) 74–78.
[5] W. Jiang, X. Gao, Y. Guo, X. Chen, Y. Zhao, Dynamic impact behavior and deformation mechanisms of Cr26Mn20Fe20Co20Ni14 high-entropy alloy, Mater. Sci. Eng. A 824 (2021) 141858.
[6] S.H. Joo, H. Kato, M.J. Jang, J. Moon, E.B. Kim, S.J. Hong, H.S. Kim, Structure and properties of ultrafine-grained CoCrFeMnNi high-entropy alloys produced by mechanical alloying and spark plasma sintering, J. Alloy. Compd. 698 (2017) 591–604.
[7] N. Choi, V. Kulitckii, J. Kottke, B. Tas, J. Choe, J.H. Yu, S. Yang, J.H. Park, J.S. Lee, G. Wilde, S.V. Divinski, Analyzing the 'non-equilibrium state' of grain boundaries in additively manufactured high-entropy CoCrFeMnNi alloy using tracer diffusion measurements, J. Alloy. Compd. 844 (2020) 155757.
[8] W.E. Frazier, Metal additive manufacturing: a review, J. Mater. Eng. Perform. 23 (6) (2014) 1917–1928.
[9] C. Tan, Q. Li, X. Yao, L. Chen, J. Su, F.L. Ng, Y. Liu, T. Yang, Y. Chew, C.T. Liu, T. DebRoy, Machine learning customized novel material for energy-efficient 4D printing, Adv. Sci. 10 (10) (2023) 2206607.
[10] C. Tan, R. Li, J. Su, D. Du, Y. Du, B. Attard, Y. Chew, H. Zhang, E.J. Lavernia, Y. Fautrelle, J. Teng, A. Dong, Review on field assisted metal additive manufacturing, Int J Mach Tool Manu 189 (2023) 104032.
[11] G. Yang, Y. Xie, S. Zhao, L. Qin, X. Wang, B. Wu, Quality control: internal defects formation mechanism of selective laser melting based on laser-powder-melt pool interaction: a review, Chinese Journal of Mechanical Engineering: Additive Manufacturing Frontiers 1 (3) (2022) 100037.
[12] D. Zhang, D. Qiu, M.A. Gibson, Y. Zheng, H.L. Fraser, D.H. StJohn, M.A. Easton, Additive manufacturing of ultrafine-grained high-strength titanium alloys, Nature 576 (7785) (2019) 91–95.
[13] G. Wang, H. Ouyang, C. Fan, Q. Guo, Z. Li, W. Yan, Z. Li, The origin of high-density dislocations in additively manufactured metals, Materials Research Letters 8 (8) (2020) 283–290.
[14] A. Birnbaum, J. Steuben, E. Barrick, A. Iliopoulos, J. Michopoulos, Intrinsic strain aging, Σ3 boundaries, and origins of cellular substructure in additively manufactured 316L, Addit. Manuf. 29 (2019).
[15] A.J. Birnbaum, J.C. Steuben, E.J. Barrick, A.P. Iliopoulos, J.G. Michopoulos, Intrinsic strain aging, Σ3 boundaries, and origins of cellular substructure in additively manufactured 316L, Addit. Manuf. 29 (2019) 100784.
[16] Y. Hong, C. Zhou, Y. Zheng, L. Zhang, J. Zheng, X. Chen, B. An, Formation of strain-induced martensite in selective laser melting austenitic stainless steel, Mater. Sci. Eng. A 740–741 (2019) 420–426.
[17] Z.G. Zhu, X.H. An, W.J. Lu, Z.M. Li, F.L. Ng, X.Z. Liao, U. Ramamurty, S.M.L. Nai, J. Wei, Selective laser melting enabling the hierarchically heterogeneous microstructure and excellent mechanical properties in an interstitial solute strengthened high entropy alloy, Materials Research Letters 7 (11) (2019) 453–459.
[18] Y.-K. Kim, S. Yang, K.-A. Lee, Compressive creep behavior of selective laser melted CoCrFeMnNi high-entropy alloy strengthened by in-situ formation of nano-oxides, Addit. Manuf. 36 (2020) 101543.
[19] B. Dovgyy, A. Piglione, P.A. Hooper, M.-S. Pham, Comprehensive assessment of the printability of CoNiCrFeMn in laser powder bed fusion, Mater. Des. 194 (2020) 108845.
[20] Y.-K. Kim, J. Choe, K.-A. Lee, Selective laser melted equiatomic CoCrFeMnNi high-entropy alloy: Microstructure, anisotropic mechanical response, and multiple strengthening mechanism, J. Alloy. Compd. 805 (2019) 680–691.
[21] B. Wang, M. Sun, B. Li, L. Zhang, B. Lu, Anisotropic response of CoCrFeMnNi high-entropy alloy fabricated by selective laser melting, Materials 13 (24) (2020) 5687.
[22] Y.-K. Kim, S. Yang, K.-A. Lee, Superior temperature-dependent mechanical properties and deformation behavior of equiatomic CoCrFeMnNi high-entropy alloy additively manufactured by selective laser melting, Sci. Rep. 10 (1) (2020) 8045.
[23] H. Chen, K. Kosiba, T. Lu, N. Yao, Y. Liu, Y. Wang, K.G. Prashanth, C. Suryanarayana, Hierarchical microstructures and strengthening mechanisms of nano-TiC reinforced CoCrFeMnNi high-entropy alloy composites prepared by laser powder bed fusion, J. Mater. Sci. Technol. 136 (2023) 245–259.
[24] X. Wang, X. Pan, P. Sun, C. Qiu, Significant enhancement in tensile strength and work hardening rate in CoCrFeMnNi by adding TiAl particles via selective laser melting, Mater. Sci. Eng. A 831 (2022) 142285.
[25] P.P. Bhattacharjee, G.D. Sathiaraj, M. Zaid, J.R. Gatti, C. Lee, C.-W. Tsai, J.-W. Yeh, Microstructure and texture evolution during annealing of equiatomic CoCrFeMnNi high-entropy alloy, J. Alloy. Compd. 587 (2014) 544–552.
[26] Y.C. Hsu, C.L. Li, C.H. Hsueh, Effects of al addition on microstructures and mechanical properties of CoCrFeMnNiAl(x), High Entropy Alloy Films, Entropy (basel) 22 (1) (2019).
[27] Y. Yang, T. Chen, L. Tan, J.D. Poplawsky, K. An, Y. Wang, G.D. Samolyuk, K. Littrell, A.R. Lupini, A. Borisevich, E.P. George, Bifunctional nanoprecipitates

strengthen and ductilize a medium-entropy alloy, Nature 595 (7866) (2021) 245–249.
[28] J. Zhang, X. Ding, R. Chen, J. Zhang, Corrosion behaviors of hot-extruded Mg96Y2Zn2 alloy in transverse and longitudinal directions: guidance for parameters selection, J. Alloy. Compd. 923 (2022) 166405.
[29] H. Zhang, L. Zhang, X. Liu, Q. Chen, Y. Xu, Effect of Zr addition on the microstructure and mechanical properties of CoCrFeNiMn high-entropy alloy synthesized by spark plasma sintering, Entropy (2018).
[30] Y. Tang, D.Y. Li, Dynamic response of high-entropy alloys to ballistic impact, Science Advances 8(32) eabp9096.
[31] M. Choi, I. Ondicho, N. Park, N. Tsuji, Strength–ductility balance in an ultrafine-grained non-equiatomic Fe50(CoCrMnNi)50 medium-entropy alloy with a fully recrystallized microstructure, J. Alloy. Compd. 780 (2019) 959–966.
[32] S. Plimpton, Fast parallel algorithms for short-range molecular dynamics, J. Comput. Phys. 117 (1) (1995) 1–19.
[33] E. Ghazvinian, M.S. Diederichs, R. Quey, 3D random Voronoi grain-based models for simulation of brittle rock damage and fabric-guided micro-fracturing, J. Rock Mech. Geotech. Eng. 6 (6) (2014) 506–521.
[34] W.-M. Choi, Y.H. Jo, S.S. Sohn, S. Lee, B.-J. Lee, Understanding the physical metallurgy of the CoCrFeMnNi high-entropy alloy: an atomistic simulation study, npj Comput. Mater. 4 (1) (2018) 1.
[35] A. Stukowski, Visualization and analysis of atomistic simulation data with OVITO–the Open visualization tool, Model. Simul. Mater. Sci. Eng. 18 (1) (2010) 015012.
[36] A. Stukowski, Structure identification methods for atomistic simulations of crystalline materials, Model. Simul. Mater. Sci. Eng. 20 (4) (2012) 045021.
[37] A. Stukowski, V.V. Bulatov, A. Arsenlis, Automated identification and indexing of dislocations in crystal interfaces, Model. Simul. Mater. Sci. Eng. 20 (8) (2012) 085007.
[38] R. Cunningham, C. Zhao, N. Parab, C. Kantzos, J. Pauza, K. Fezzaa, T. Sun, A. D. Rollett, Keyhole threshold and morphology in laser melting revealed by ultrahigh-speed x-ray imaging, Science 363 (6429) (2019) 849–852.
[39] M.H. Mosallanejad, B. Niroumand, A. Aversa, A. Saboori, In-situ alloying in laser-based additive manufacturing processes: a critical review, J. Alloy. Compd. 872 (2021) 159567.
[40] P. Tan, R. Kiran, K. Zhou, Effects of sub-atmospheric pressure on keyhole dynamics and porosity in products fabricated by selective laser melting, J. Manuf. Process. 64 (2021) 816–827.
[41] D. Kong, C. Dong, S. Wei, X. Ni, L. Zhang, R. Li, L. Wang, C. Man, X. Li, About metastable cellular structure in additively manufactured austenitic stainless steels, Addit. Manuf. 38 (2021) 101804.
[42] X. Zhou, K. Li, D. Zhang, X. Liu, J. Ma, W. Liu, Z. Shen, Textures formed in a CoCrMo alloy by selective laser melting, J. Alloy. Compd. 631 (2015) 153–164.
[43] P. Lejček, M. Roudnická, J. Čapek, D. Dvorský, J. Drahokoupil, D. Šimek, J. Čížek, P. Svora, O. Molnárová, D. Vojtěch, Selective laser melting of pure iron: multiscale characterization of hierarchical microstructure, Mater Charact 154 (2019) 222–232.
[44] I. Ondicho, M. Choi, W.-M. Choi, J.B. Jeon, H.R. Jafarian, B.-J. Lee, S.I. Hong, N. Park, Experimental investigation and phase diagram of CoCrMnNi–Fe system bridging high-entropy alloys and high-alloyed steels, J. Alloy. Compd. 785 (2019) 320–327.
[45] R. Li, P. Niu, T. Yuan, P. Cao, C. Chen, K. Zhou, Selective laser melting of an equiatomic CoCrFeMnNi high-entropy alloy: processability, non-equilibrium microstructure and mechanical property, J. Alloy. Compd. 746 (2018) 125–134.
[46] Z.G. Zhu, Q.B. Nguyen, F.L. Ng, X.H. An, X.Z. Liao, P.K. Liaw, S.M.L. Nai, J. Wei, Hierarchical microstructure and strengthening mechanisms of a CoCrFeNiMn high entropy alloy additively manufactured by selective laser melting, Scr. Mater. 154 (2018) 20–24.
[47] Y.H. Zhou, Z.H. Zhang, Y.P. Wang, G. Liu, S.Y. Zhou, Y.L. Li, J. Shen, M. Yan, Selective laser melting of typical metallic materials: an effective process prediction model developed by energy absorption and consumption analysis, Addit. Manuf. 25 (2019) 204–217.
[48] S. Guan, D. Wan, K. Solberg, F. Berto, T. Welo, T.M. Yue, K.C. Chan, Additive manufacturing of fine-grained and dislocation-populated CrMnFeCoNi high entropy alloy by laser engineered net shaping, Mater. Sci. Eng. A 761 (2019) 138056.
[49] Y. Chew, G.J. Bi, Z.G. Zhu, F.L. Ng, F. Weng, S.B. Liu, S.M.L. Nai, B.Y. Lee, Microstructure and enhanced strength of laser aided additive manufactured CoCrFeNiMn high entropy alloy, Mater. Sci. Eng. A 744 (2019) 137–144.
[50] S. Xiang, H. Luan, J. Wu, K.-F. Yao, J. Li, X. Liu, Y. Tian, W. Mao, H. Bai, G. Le, Q. Li, Microstructures and mechanical properties of CrMnFeCoNi high entropy alloys fabricated using laser metal deposition technique, J. Alloy. Compd. 773 (2019) 387–392.
[51] Z. Tong, X. Ren, J. Jiao, W. Zhou, Y. Ren, Y. Ye, E.A. Larson, J. Gu, Laser additive manufacturing of FeCrCoMnNi high-entropy alloy: effect of heat treatment on microstructure, residual stress and mechanical property, J. Alloy. Compd. 785 (2019) 1144–1159.
[52] M.A. Melia, J.D. Carroll, S.R. Whetten, S.N. Esmaeely, J. Locke, E. White, I. Anderson, M. Chandross, J.R. Michael, N. Argibay, E.J. Schindelholz, A.B. Kustas, Mechanical and corrosion properties of additively manufactured CoCrFeMnNi high entropy alloy, Addit. Manuf. 29 (2019) 100833.
[53] J.Y. He, W.H. Liu, H. Wang, Y. Wu, X.J. Liu, T.G. Nieh, Z.P. Lu, Effects of Al addition on structural evolution and tensile properties of the FeCoNiCrMn high-entropy alloy system, Acta Mater. 62 (2014) 105–113.
[54] S.J. Sun, Y.Z. Tian, H.R. Lin, X.G. Dong, Y.H. Wang, Z.J. Zhang, Z.F. Zhang, Enhanced strength and ductility of bulk CoCrFeMnNi high entropy alloy having fully recrystallized ultrafine-grained structure, Mater. Des. 133 (2017) 122–127.
[55] M.V. Klimova, A.O. Semenyuk, D.G. Shaysultanov, G.A. Salishchev, S. V. Zherebtsov, N.D. Stepanov, Effect of carbon on cryogenic tensile behavior of CoCrFeMnNi-type high entropy alloys, J. Alloy. Compd. 811 (2019) 152000.
[56] J.H. Kim, K.R. Lim, J.W. Won, Y.S. Na, H.-S. Kim, Mechanical properties and deformation twinning behavior of as-cast CoCrFeMnNi high-entropy alloy at low and high temperatures, Mater. Sci. Eng. A 712 (2018) 108–113.
[57] Y.-K. Kim, J.-H. Yu, H.S. Kim, K.-A. Lee, In-situ carbide-reinforced CoCrFeMnNi high-entropy alloy matrix nanocomposites manufactured by selective laser melting: carbon content effects on microstructure, mechanical properties, and deformation mechanism, Compos. B Eng. 210 (2021) 108638.
[58] H. Shahmir, J. He, Z. Lu, M. Kawasaki, T.G. Langdon, Effect of annealing on mechanical properties of a nanocrystalline CoCrFeNiMn high-entropy alloy processed by high-pressure torsion, Mater. Sci. Eng. A 676 (2016) 294–303.
[59] G. Laplanche, A. Kostka, O.M. Horst, G. Eggeler, E.P. George, Microstructure evolution and critical stress for twinning in the CrMnFeCoNi high-entropy alloy, Acta Mater. 118 (2016) 152–163.
[60] N. Eißmann, B. Klöden, T. Weißgärber, B. Kieback, High-entropy alloy CoCrFeMnNi produced by powder metallurgy, Powder Metall. 60 (3) (2017) 184–197.
[61] D. Riabov, A. Leicht, J. Ahlström, E. Hryha, Investigation of the strengthening mechanism in 316L stainless steel produced with laser powder bed fusion, Mater. Sci. Eng. A 822 (2021) 141699.
[62] E. Liverani, S. Toschi, L. Ceschini, A. Fortunato, Effect of selective laser melting (SLM) process parameters on microstructure and mechanical properties of 316L austenitic stainless steel, J. Mater. Process. Technol. 249 (2017) 255–263.
[63] X. Wang, J.A. Muñiz-Lerma, O. Sánchez-Mata, M. Attarian Shandiz, M. Brochu, Microstructure and mechanical properties of stainless steel 316L vertical struts manufactured by laser powder bed fusion process, Mater. Sci. Eng. A 736 (2018) 27–40.
[64] D.-H. Ping, Understanding solid-solid (fcc → ω + bcc) transition at atomic scale, Acta Metallurgica Sinica (english Letters) 28 (2015).
[65] P. Shi, W. Ren, T. Zheng, Z. Ren, X. Hou, J. Peng, P. Hu, Y. Gao, Y. Zhong, P. K. Liaw, Enhanced strength–ductility synergy in ultrafine-grained eutectic high-entropy alloys by inheriting microstructural lamellae, Nat. Commun. 10 (1) (2019) 489.
[66] U.F. Kocks, H. Mecking, Physics and phenomenology of strain hardening: the FCC case, Prog. Mater Sci. 48 (3) (2003) 171–273.
[67] S. Asgari, E. El-Danaf, S.R. Kalidindi, R.D. Doherty, Strain hardening regimes and microstructural evolution during large strain compression of low stacking fault energy fcc alloys that form deformation twins, Metall. Mater. Trans. A 28 (9) (1997) 1781–1795.
[68] K.M. Rahman, V.A. Vorontsov, D. Dye, The effect of grain size on the twin initiation stress in a TWIP steel, Acta Mater. 89 (2015) 247–257.
[69] Y.T. Zhu, X.Z. Liao, X.L. Wu, J. Narayan, Grain size effect on deformation twinning and detwinning, J. Mater. Sci. 48 (13) (2013) 4467–4475.
[70] B.C. De Cooman, Y. Estrin, S.K. Kim, Twinning-induced plasticity (TWIP) steels, Acta Mater. 142 (2018) 283–362.
[71] H.-U. Jeong, N. Park, TWIP and TRIP-associated mechanical behaviors of Fex (CoCrMnNi)100–x medium-entropy ferrous alloys, Mater. Sci. Eng. A 782 (2020) 138896.
[72] D. Molnár, X. Sun, S. Lu, W. Li, G. Engberg, L. Vitos, Effect of temperature on the stacking fault energy and deformation behaviour in 316L austenitic stainless steel, Mater. Sci. Eng. A 759 (2019) 490–497.
[73] V. Yamakov, D. Wolf, S.R. Phillpot, A.K. Mukherjee, H. Gleiter, Dislocation processes in the deformation of nanocrystalline aluminium by molecular-dynamics simulation, Nat. Mater. 1 (1) (2002) 45–49.
[74] D. Utt, S. Lee, Y. Xing, H. Jeong, A. Stukowski, S.H. Oh, G. Dehm, K. Albe, The origin of jerky dislocation motion in high-entropy alloys, Nat. Commun. 13 (1) (2022) 4777.